

# Specular reflectance of optical-black coatings in the far infrared

Sheldon M. Smith

Far-infrared specular reflectance spectra of seven optically black coatings near normal incidence are presented. Seven photometric spectra were obtained using eleven bandpass transmission filters in the wavelength range between 12 and 500  $\mu\text{m}$ , and three interferometric spectra were obtained for corroboration. Data on the construction, thickness, and rms surface roughness of the coatings are also presented. The chemical composition of three coatings can be distinguished from that of the others by a strong absorption feature between 20 and 40  $\mu\text{m}$ , which can be largely attributed to amorphous silicate material. At 100  $\mu\text{m}$ , the most and least reflective coatings differ by nearly 3 orders of magnitude. Inverse relationships observed between the spectra and the roughness and thickness of the coatings led to development of a reflecting-layer model for the measured reflectance. The model successfully describes the spectra at wavelengths outside the silicate absorption, and optical constants are deduced from a nonlinear least squares fit to the data. Parametric errors are estimated by chi-square analysis, and sensitivity tests are performed to determine which parameters control reflectance in different spectral regions.

## I. Introduction

Most optically black coatings consist of a visibly absorbing dielectric of mean thickness  $d$  and rms surface roughness  $\sigma$  applied to a smooth metallic surface. The solution of the wave equation in an absorbing dielectric<sup>1</sup> with imaginary refractive index  $k$  has an exponential dependence on the optical depth,  $4\pi kd/\lambda$ , and when this becomes small the reflectance of a coated surface increases. Roughening a coating attenuates an incident plane wave through scattering; Bennett and Porteus<sup>2</sup> have shown that the hemispheric diffuse reflectance of a rough conducting surface is proportional to  $(4\pi\sigma/\lambda)^2$ . Thus the attenuating effect of an optical-black coating can be expected to decrease nonlinearly with decreasing values of  $d/\lambda$  and  $\sigma/\lambda$ . Conversely, the specular reflectance of a coating of specified thickness and roughness may be expected to increase with wavelength in the far IR.

Because stray-light rejection is very important in the design of the Shuttle Infrared Telescope Facility (SIRTF) (a cryogenically cooled telescope intended to operate between 1 and 700  $\mu\text{m}$ ), this study was undertaken to quantify the expected increase of the far-IR reflectance of optical-black coatings. The results reported here pertain only to the normal incidence spec-

ular reflectance and not to other properties important for space applications. In particular, these results should not be construed to mean that one coating is best, because no single coating can satisfy the performance criteria of all optical applications.

The next section of this paper describes the instrumentation, while Sec. III presents and discusses the far-IR spectra. In Sec. IV, an equation is developed for the specular reflectance of rough thick coatings near normal incidence, and in Sec. V the parameters of the equation are adjusted to provide a least squares fit to the measured spectra. In the final section the dominant parameters in different spectral regions are determined by individual adjustment of each parameter.

## II. Nonspecular Reflectometer

### A. Mechanical and Optical Layout

The mechanical and optical layout is shown schematically in Fig. 1. An  $f/33$  ellipsoid of revolution images a 1500 K blackbody source inside the detector's field stop following specular reflection from the substrate. Although this paper is limited to specular reflection at nearly normal incidence, the nonspecular reflectometer (NSR) is capable of making nonspecular measurements at scattering angles  $\theta_s$  between 6 and  $\pm 90^\circ$  with angles of incidence  $\theta_i$  of  $6^\circ$  or larger. Some of those nonspecular bidirectional reflectance (BRDF) measurements<sup>3</sup> are reported elsewhere. During most of these measurements ambient conditions existed along the 1-m optic path, and the detector field stop subtended just  $1.94^\circ$  at the substrate.

The author is with NASA Ames Research Center, Moffett Field, California 94035.

Received 11 March 1983.

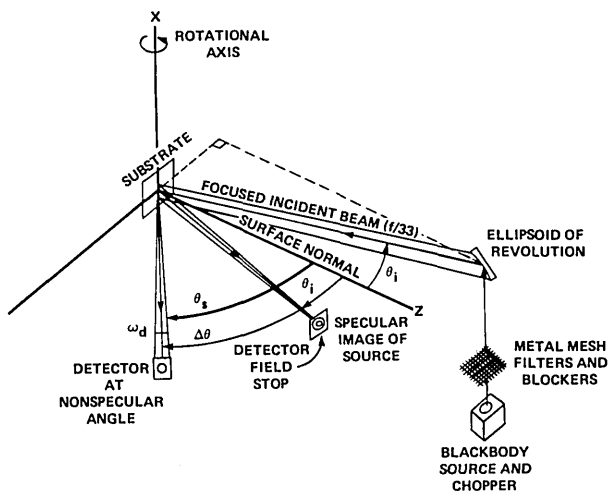


Fig. 1. Schematic drawing of the nonspecular reflectometer (NSR).

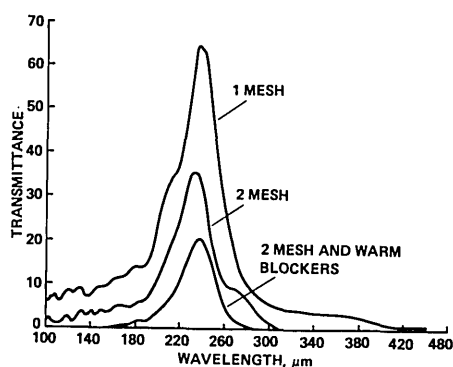


Fig. 2. Mesh filter transmission: (a) single inductive mesh with wire spacing of 120 wires/in.; (b) pair of 120 mesh separated 25 mm or more; (c) same pair of mesh with room temperature blocking filters of 0.1-mm black polyethylene, 0.75-mm z-cut crystal quartz with roughened surfaces, and a longwave pass interference filter (HERA) from Whitcomb and Keene.<sup>6</sup>

## B. Filters

The filter at 12  $\mu\text{m}$  is a commercially available interference filter with an effective spectral resolution of 2%. The twelve other filters are basically incoherent pairs of electroformed nickel mesh<sup>4</sup> used in transmission. As suggested by Sakai and Yoshida,<sup>5</sup> the mesh has a wire width which is exactly one-half of the wire spacing. Figure 2 shows the transmission of a representative pair. When separated  $\sim 25$  mm or more, coherent reflection between the individual meshes becomes small. Hence the incoherent transmission of a pair is approximately the square of the transmission of a single mesh. Table I lists the principal characteristics of the filters used in the NSR. The peak transmissions listed are adequate for specular reflectance measurements, although the transmission of two filters is disappointingly low.

The wavelength response of the NSR is determined by the product of filter transmission and source emittance because the detector, a bolometer, is relatively independent of wavelength. Because the filters are in the Rayleigh-Jeans region of the 1500 K source spectrum, photometrically effective passbands (half-power points) were determined from graphs of  $\lambda^{-4}T(\lambda)$ . Photometrically effective wavelengths were obtained from

$$\int \lambda T(\lambda) B(\lambda, T) d\lambda / \int T(\lambda) B(\lambda, T) d\lambda, \quad (1)$$

where  $T(\lambda)$  represents the transmission of all filters in the beam, and  $B(\lambda, T)$  is the Planck function. These effective quantities are listed in columns 4 and 5 of Table I. As would be expected with a  $\lambda^{-4}$  weighting function, the effective  $\lambda$  is generally smaller than the peak  $\lambda$  of the filter alone. In the case of the last filter, which was intended to operate near 320  $\mu\text{m}$ , the shift is so large and the effective passband so broad that the filter is nearly useless; its data were not used in the curve fitting discussed in Sec. V.

Table I. Characteristics of Incoherent Pairs of Mesh Filters with Blocking

Peak wavelength ( $\mu\text{m}$ )	Mesh size <sup>a</sup> (wires/in.)	Approximate peak transmission <sup>b</sup> (%)	Effective half-power points ( $\mu\text{m}$ )	Effective wavelength ( $\mu\text{m}$ )	Effective resolution <sup>c</sup>
12.2	Interference	70	12.1 $\rightarrow$ 12.4	12.2	0.02
29.5	1000	18	26.5 $\rightarrow$ 31.7	31.4	0.17
36.5	750	17	33.1 $\rightarrow$ 38.3	35.1	0.15
68.5	400	12	60.0 $\rightarrow$ 72.0	66.0	0.18
110	250	21	102 $\rightarrow$ 118	109.5	0.15
166	150	4	140 $\rightarrow$ 181	164	0.25
235	120	22	211 $\rightarrow$ 249	218	0.17
290	90	12	220 $\rightarrow$ 320	262	0.38
320	80	4	137 $\rightarrow$ 335	237	0.83
Additional filters for ECP-2200:					
18	1500	20	17.8 $\rightarrow$ 19.4	18.5	0.09
235	120	22	221 $\rightarrow$ 248	234	0.12
290	90	9	296 $\rightarrow$ 353	334	0.17
500	55	20	420 $\rightarrow$ 520	470	0.21

<sup>a</sup> Wire width to wire spacing ratio =  $1/2$ .

<sup>b</sup> Does not include losses due to cold blocking filters.

<sup>c</sup> Resolution =  $\Delta\lambda$  of half-power points/effective wavelength.

With the blackbody source at 1500 K, short-wavelength radiation must be attenuated by nearly 6 orders of magnitude to use filters at wavelengths beyond 100  $\mu\text{m}$ . Several combinations of black polyethylene, cold sapphire, diamond dust, roughened quartz, KRS-6, and various alkali halides are used to produce this amount of blocking for the different filter bands. Beyond 160  $\mu\text{m}$ , we are particularly fortunate to have a longwave pass interference filter made by Whitcomb and Keene<sup>6</sup> which reduces some of the reflection loss from the many surfaces of the usual collection of blocking filters. Since thermal background blockers must operate at liquid helium temperature, they are mounted on a twelve-position filter-carousel inside the detector Dewar. Most of the warm filters are scattering filters so they are mounted just above the source aperture, far from the detector. Because the filters are separated in this way, the total transmission of each combination was not measured. However, the spectral purity of each filter band has been tested in three ways: first, by inserting an additional piece of black polyethylene into the beam; second, by inserting additional but similar filters; and, third, by inserting dissimilar filters. The short-wavelength leak of the mesh itself, as shown in Fig. 2, is characteristic of inductive mesh.<sup>7</sup> On other spectra of this combination, the leak is blocked by the warm filters to transmission levels below  $3 \times 10^{-4}$  down to a wavelength of 20  $\mu\text{m}$ . In addition to the warm filters listed in the caption of Fig. 2, another piece of 0.1-mm black polyethylene and a 1-mm thick piece of  $\text{CaF}_2$  with diamond dust coating on both surfaces<sup>8</sup> are located inside the detector Dewar to reduce radiant heating of the detector by the ambient 300 K thermal background. Similar combinations are used with the other mesh pairs.

### C. Detector

The detector is a liquid-helium-cooled gallium-doped germanium bolometer that is operated at a constant bias current of 3  $\mu\text{A}$ . Its helium bath is pumped to  $\sim 16$  Torr to reduce the operating temperature below 2 K. At this temperature NEP is  $\sim 7 \times 10^{-14} \text{ W}/\sqrt{\text{Hz}}$ . The Dewar has a 1-mm thick white polyethylene window and a twelve-position filter-carousel which rotates a selected thermal blocker across the incident beam just before the detector field stop. An  $f/12$  off-axis field mirror (not shown in Fig. 1) is mounted directly behind the field stop. It images the entire 25-mm square reflectance substrate within the edge of the 2-mm diam germanium detector chip. The chopped source is synchronously detected by a phase-lock amplifier operating near 20 Hz. This arrangement detects signals down to the noise level near  $10^{-7} \text{ V}$  with time constants near 300 msec. A further order of magnitude increase in detectability is available by time-averaging the amplifier output on an external microprocessor circuit.

### D. Measurements

The absolute spectral reflectance of a coating at effective wavelength  $\lambda$  is measured relative to the power reflected from a gold-coated glass mirror placed in the

same position and assumed to have 100% reflectivity. This definition reduces the dependence of the measured reflectance on the filter's spectral bandwidth to a few percent or less when the measured spectrum is reasonably linear across the passband, and the filter's resolution is better than 40%.

The photometric spectra reported in the following section are generally consistent with the spectral measurements made by Grammer *et al.*<sup>9</sup> of several similar coatings. Of course, these specular measurements give smaller values than the total hemispheric reflectance measurements of Pipher and Houck<sup>10</sup> and of Stierwalt.<sup>11</sup> In view of the relatively deep interference fringes demonstrated by several coatings in the next section, these broadband results should not be expected to agree very well with specular measurements made on other reflectometers, particularly those using narrow-band lasers. However, when two such comparisons were made, the results were found to agree to within 15%, which was most fortuitous. One comparison, however, is significant. That comparison is between the 28- $\mu\text{m}$   $\text{CO}_2$  laser measurement by Compton *et al.*<sup>12</sup> of an  $\sim 70$ - $\mu\text{m}$  thick coating of 3M Black Velvet (Nextel 101-C10 in spray cans) and our 31.4- $\mu\text{m}$  filter measurement of a 66- $\mu\text{m}$  thick coating of the same material. Both measurements found the specular reflectance near normal incidence to be  $< 10^{-4}$  because of the broad absorption feature between 15 and 40  $\mu\text{m}$  discussed in the next section.

### E. Sample Preparation

All but one of the black coatings tested were applied by the originator or manufacturer of the coating: 2.54-cm (1-in.) square substrates of 7075-T6 aluminum were lapped optically flat at Ames Research Center and then mailed in plastic containers to the coating originators, who applied the coatings to the substrates and returned them. The 3M Black Velvet coating was applied by the author. It was impossible to obtain a uniform coat with a single spraying. Two sprayings, each at an incidence angle of  $\sim 30^\circ$  but  $180^\circ$  apart in azimuth, produced a visually uniform coating apparently free of pinholes.

## III. Spectra of Optical-Black Coatings

This section presents far-infrared specular reflectance measurements<sup>13</sup> of seven optically black coatings and discusses their salient features. Pertinent information regarding coating construction, rms surface roughness, and coating thickness are presented in Table II. Roughness was measured on commercial profilometers for all coatings except Cornell Black, which had to be measured by visual and tactile comparisons with a metal roughness standard (General Electric 8651831G2). Thickness was measured on photomicrographs of the edge of the samples.

Table II illustrates several important characteristics of these coatings. First, note that carbon black is an ingredient common to five of the seven coatings. Also note the diversity in design. Attenuation techniques range from simple black pigmentation, through anodi-

Table II. Optical-Black Coatings

Coating name (industry contact)	Construction technique	$\sigma$ ( $\mu\text{m}$ )	$d$ ( $\mu\text{m}$ )
Chemglaze Z-306 (S. A. Slawiak)	Carbon-black pigmented polyurethane coating	2	40
IITRI D-111 (J. Brzuskiwicz)	Carbon-black pigmented potassium silicate coating	3	48
3M ECP-2200 (B. A. Benson)	Jagged silica particles in a silicone binder containing a proprietary black dye	4	55
Martin Black (S. M. Pompea)	Chemically anodized aluminum containing a proprietary black dye	8	>50
3M Black Velvet Nextel 101-C10 (L. L. Olson)	Carbon-black-coated solid silicate spheres (8–20- $\mu\text{m}$ diam) applied as a spray	7	66
Cornell Black (J. R. Houck)	3M Black Velvet loaded with SiC grinding grit of 200– 300- $\mu\text{m}$ major dimension	~30	96
LMSC Black (J. R. Grammer)	Thick multilayer coating composed of several polyurethane layers containing increasing amounts of carbon-black pigment	~1	200

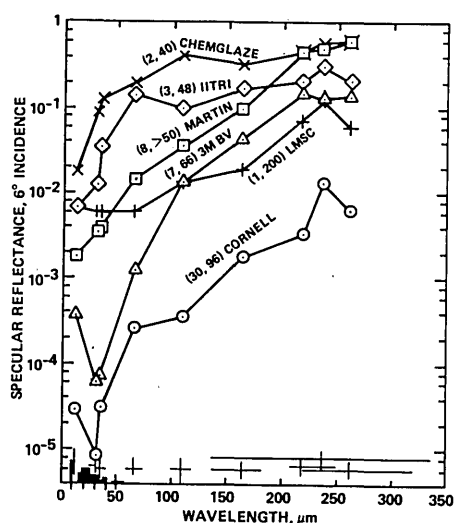


Fig. 3. Photometric reflectance spectra of six optical-black coatings. The specular reflectance at 6° incidence angle was measured with a detector that subtended  $9.02 \times 10^{-4}$  sr at the substrate. The principal absorption bands of amorphous silicate material<sup>14</sup> are shown schematically in the lower left corner. Coating roughness and thickness are given in parentheses ( $\sigma, d$ ).

zation, to multilayer construction with a refractive-index gradient. One coating, 3M Black Velvet (BV), is also used as a primary ingredient in another coating, Cornell Black. This point will be noted again shortly.

Photometric reflectance spectra of six coatings are shown in Fig. 3, where the individual data points have been connected by straight lines, and errors bars are shown below the spectra to prevent clutter. The photometric spectrum of 3M ECP-2200 is not included in this figure because it was not obtained under the same (ambient) conditions as these spectra. The horizontal

error bars are the effective half-power bandwidths given in Table I. The vertical error bars represent a total absolute error estimate and not just statistical uncertainty. They were derived from the maximum variations observed during our first experience with the NSR and result largely from internal uncertainties associated with angular alignment, detector response, and atmospheric transmission along the ambient 1-m optic path. The histogram (at the lower left corner of the figure) represents schematically the mass absorption coefficient of amorphous magnesium silicate material prepared and measured by Day.<sup>14</sup>

The most significant feature of these spectra is the tremendous variation evident in the measured specular reflectance. At wavelengths near 100  $\mu\text{m}$ , the reflectance differs by nearly 3 orders of magnitude.

Note also the different dependence on wavelength shown by several coatings. The reflectance of the upper two coatings in Fig. 3 (simple pigmented types) rises rapidly with increasing wavelength. The reflectance of the middle coating (Martin, black anodized aluminum) rises more slowly, rather monotonically with wavelength. LMSC Black (the multilayered coating) has a totally different wavelength dependence; its spectrum rises so slowly it cuts across three other spectra.

The lower two coatings in Fig. 3 show a similar spectral absorption feature between 30 and 40  $\mu\text{m}$ . This strong absorption was also seen in 3M BV at 28  $\mu\text{m}$  by Compton *et al.*<sup>12</sup> and between 18 and 40  $\mu\text{m}$  in our photometric spectrum of ECP-2200 (Fig. 11). It is not surprising that both coatings in Fig. 3 have this feature since they both contain 3M BV. Furthermore, J. R. Grammer (personal communication) has found that 3M BV is made of carbon-black-coated solid spheres of silicate material. Thus the deep short-wavelength absorption of these two coatings can be largely attributed to the principal bands of amorphous silicate material,<sup>14</sup> since the extinction spectrum of carbon black is nearly featureless in this region.<sup>15</sup> This deduction is supported further by the appearance of the feature in the photometric spectrum of ECP-2200, which contains silicates but not carbon black. The feature may be enhanced in Cornell Black by the addition of amorphous SiC, since pure SiC has both vibrational and lattice bands in the 10–13- $\mu\text{m}$  region.<sup>16</sup>

Fourier transform interferometer spectra of ECP-2200 and of two of the same samples shown in Fig. 3 are shown in Fig. 4 on a relative scale. The spectra were measured at 17° incidence with a resolution of  $8 \text{ cm}^{-1}$  by R. V. Howitt (Santa Barbara Research Center, Goleta, Calif.) by installing a reflectance attachment in the Nicolet 8000 interferometer. The angle subtended by the instrument's detectors was  $\sim 2.3^\circ$ , quite similar to that of the NSR.

These high resolution spectra show clear evidence of interference fringes not apparent in the previous photometric measurements of the same samples. In non-absorbing films such effects are commonly referred to as channel spectra. As might be expected, the multilayer coating (LMSC) exhibits them the most clearly. Such effects have also been observed by Grammer *et al.*<sup>9</sup>

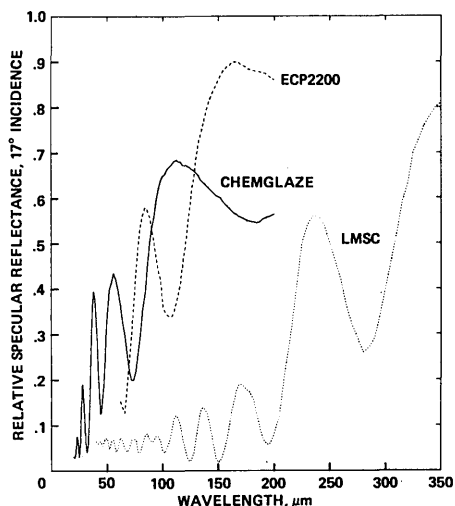


Fig. 4. Interferometric relative reflectance spectra measured at 17° incidence at the Santa Barbara Research Center with detectors subtending  $\sim 1.2 \times 10^{-3}$  sr at the substrate.

in the reflectance of Martin Black, IITRI D-111, and some other relatively thin coatings not studied here.

Returning to Fig. 3, the surface roughness and thickness in microns are shown in parentheses ( $\sigma, d$ ) before the name of each coating. Scanning from the top of the figure down at wavelengths near 100  $\mu\text{m}$  reveals a roughly inverse dependence of reflectance on roughness. (LMSC Black is excluded from these considerations because of its unusual construction.) Further examination of Fig. 3 also reveals an apparently inverse dependence on thickness at far-infrared wavelengths. These two trends led to development of the simple reflecting layer model described in the next section. The value of such a model is that it can be used to identify parameters important in the design of highly attenuating coatings.

#### IV. Reflecting-Layer Model

A rigorous solution for the electromagnetic wave reflected by a rough thick absorbing film is beyond the scope of this paper; however, a first-order evaluation based on the scalar solutions at normal incidence of two distinctly separate cases is feasible. The reflectance by an optical black or infrared opaque coating may represent a worst possible practical case in that it requires consideration of an absorbing film whose roughness and thickness may both be a significant fraction of a wavelength. The reflectance of a smooth thin dielectric film (with and without absorption) has been well developed,<sup>1,17</sup> while a scalar evaluation by Porteus<sup>18</sup> of the Kirchoff integral has produced a relatively simple expression for the reflectance of a rough conducting surface. To produce a first-order approximation of the reflectance by a rough thick absorbing coating at normal incidence, the scalar solutions from these two separate cases will be combined.

Because infrared opaque coatings are generally less than several wavelengths thick, thin film theory is more applicable to them than the thick scattering model of Kubelka-Monk.<sup>19</sup> Let us start with the development

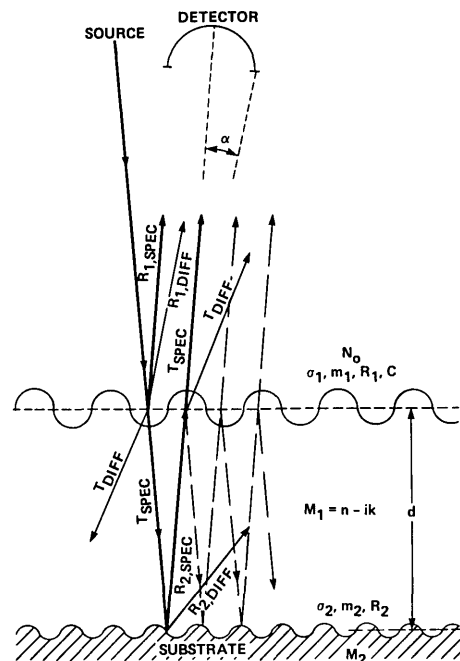


Fig. 5. Reflecting layer model.

by Heavens<sup>17</sup> for the sum of the amplitudes of successive beams reflected by a coating of complex index  $M_1$  applied to a substrate of index  $M_2$ , as shown in Fig. 5. The coating is assumed to have a uniform average thickness  $d$ , and the phase shift (also complex) of each beam after traversing once through the film is

$$\delta = \frac{2\pi}{\lambda} M_1 d = \frac{2\pi d}{\lambda} (n - ik), \quad (2)$$

where  $\lambda$  is the wavelength in vacuum. It is also assumed that the source and detector are at the specular angle closest to normal incidence. Heavens [his eq. 4(42)] gives the amplitude reflectance as

$$\mathcal{R} = r_1 + t_1 t_1' r_2 \exp(-2i\delta) - t_1 t_1' r_1 r_2^2 \exp(-4i\delta) + t_1 t_1' r_1^2 r_2^2 \exp(-6i\delta) \dots, \quad (3)$$

where  $r_1$  and  $t_1$  are the well-known Fresnel reflection and transmission coefficients of the first (upper) surface [Heavens's Eqs. 4(19) and 4(20)], and  $r_2$  is the reflection coefficient of the lower (substrate) surface. The terms of the series following the second alternate in sign because there is no change in phase at the internal reflection from the upper surface. More important, the first two terms add because they both result from external reflections. To emphasize this, Eq. (3) can be rewritten as

$$\mathcal{R} = r_1 + t_1 t_1' r_2 \exp(-2i\delta) - t_1 t_1' r_1 r_2^2 \times \exp(-4i\delta) \sum_{j=0}^{\infty} [-r_1 r_2 \exp(-2i\delta)]^j. \quad (4)$$

Since  $\delta$  is complex, each term of this amplitude series is a factor of  $\exp(-4\pi k d / \lambda)$  smaller than the preceding. Hence the sum indicated is an alternating sequence of successively smaller terms, which should rapidly converge to a small number. Thus in this first-order ap-

proximation it can be neglected compared to the sum of just the first two terms.

In Eqs. (3) and (4),  $t_1'$  is the transmission coefficient of the upper surface going from medium  $M_1$  out to medium  $N_0$ . Heavens<sup>17</sup> comments that this is not the same as  $t_1$  for transmission from  $N_0$  into  $M_1$ , but he also notes that through compensating errors in applying conservation of energy the correct result can be obtained anyhow. We will make the same error intentionally and rely on the serendipitous result from conservation of energy to simplify merging, at a later step, this thin film approximation with the result of the rough surface evaluation. Thus the power transmittance of the upper surface is defined as

$$T_1 = t_1 t_1' = t_1 t_1^*, \quad (5)$$

where the asterisk indicates the complex conjugate. Rigorous application of the Fresnel coefficients shows that the normal incidence power reflectance of the upper surface,

$$R_1 = r_1 r_1^* = \frac{(n - N_0)^2 + k^2}{(n + N_0)^2 + k^2}, \quad (6)$$

is independent of the direction of propagation through the surface. Conservation of energy (absorption in the surface being neglected) then gives

$$T_1 = 1 - R_1, \quad (7)$$

which also is independent of direction as indicated in the definition of Eq. (5).

Utilizing these definitions, the power reflectance of the entire coating as obtained from just the first two terms of Eq. (3) is then

$$R = \mathcal{R} \mathcal{R}^* = R_1 + T_1 [r_1^* r_2 \exp(-2i\delta) + r_1 r_2^* \exp(+2i\delta^*)] + T_1^2 R_2 \exp[-2i(\delta - \delta^*)], \quad (8)$$

where

$$R_2 = r_2 r_2^* \quad (9)$$

is the power reflectance of the lower surface. Defining  $r_1$  and  $r_2$  by polar coordinates in the complex plane and applying Euler's formula after some routine complex arithmetic yield

$$R = R_1 + 2T_1(R_1 R_2)^{1/2} \exp(-4\pi k d / \lambda) \cos\left(\frac{4\pi n d}{\lambda}\right) + T_1^2 R_2 \exp(-8\pi k d / \lambda), \quad (10)$$

where  $r_1 r_2 = (R_1 R_2)^{1/2}$  has been used. A phase shift owing to the difference between the phase changes upon reflection at the first and second surfaces has been neglected in the cosine term. Since the reflections at these interfaces are both external (from rare to dense), further complex arithmetic shows that for representative values of  $M_1$  and  $M_2$  both phase changes are relatively small and of the same sign. Thus their difference can be neglected relative to the large phase shift caused by coating thickness.

In Eq. (10),  $R_1$  of the first surface can be identified as the normal incidence Fresnel reflectance of the coating material itself. The third term is an absorption term, giving a measure of the attenuation of a beam after

passing twice through the coating and reflecting once off the substrate. The second term is an oscillatory interference term resulting from the cross product in  $\mathcal{R} \mathcal{R}^*$ .

The effect of rough surfaces on the reflectance of the coating described by Eq. (10) can now be addressed. To do this we extend to dielectric coatings the result of Porteus<sup>18</sup> which was obtained by application of a scalar evaluation of the Kirchhoff integral to conductors. Although more sophisticated vector evaluations are available,<sup>20,21</sup> this formulation is adequate for a first-order analysis. For  $\lambda \geq \sigma$ , Porteus has shown that at normal incidence the specular (power) reflectance measured from a metal surface by a detector with the acceptance half-angle  $\alpha$  is

$$R = R_0 (\exp[-(4\pi\sigma/\lambda)^2] + \{1 - \exp[-(4\pi\sigma/\lambda)^2]\} \times \{1 - \exp[-(\sqrt{2}\pi\alpha\sigma/m\lambda)^2]\}), \quad (11)$$

where  $R_0$  is the normal incidence reflectance of a perfectly smooth surface of the same material,  $\sigma$  is the rms roughness, and  $m$  is the rms slope of the hills or facets of the surface. We extend this result to dielectric coatings by letting  $R_0$  be the normal incidence Fresnel reflectance of the coating defined earlier in Eq. (6). Porteus employed a statistical description of the surface which assumed his normal surface, one that has Gaussian distributions of both roughness and horizontal separation and does not have excessively steep slopes. The last bracket on the right-hand side of Eq. (11) results from integration of the directional reflectance over the acceptance angle of the detector and gives the fraction of the diffuse reflectance which is detected.

Equation (11) can be separated into specular and diffuse parts. Bennett and Porteus<sup>2</sup> give the normal incidence specular reflectance as

$$R_{1\text{spec}} = R_1 \exp[-(4\pi\sigma/\lambda)^2]; \quad (12)$$

hence the diffuse reflectance into a hemisphere is

$$R_{1\text{diff}} = R_1 \{1 - \exp[-(4\pi\sigma/\lambda)^2]\}. \quad (13)$$

Bennett<sup>22</sup> and others commonly refer to  $R_{1\text{diff}}/R_1$  as the total integrated scatter (TIS). The total reflectance of the upper surface is the sum of both components:

$$R_{1\text{spec}} + R_{1\text{diff}} = R_1, \quad (14)$$

which is also consistent with the definition [Eq. (6)] of  $R_1$  as the directional-hemispheric reflectance<sup>23</sup> at normal incidence.

Diffuse reflectance at the upper surface is quite likely to be accompanied by diffuse transmission through the surface, which, as indicated by  $T_{\text{diff}}$  in Fig. 5, will remove light from the specularly transmitted beam. A correction for the diffuse transmission can be made by rewriting Eq. (7) in analogy to Eq. (14):

$$1 - R_1 = T_1 = T_{\text{spec}} + T_{\text{diff}}. \quad (15)$$

If  $T_{\text{diff}}$  is related to  $R_{\text{diff}}$  through a scattering parameter  $C$ ,

$$T_{\text{diff}} = C R_{1\text{diff}}, \quad (16)$$

then, from Eqs. (15), (16), and (13), the specular transmission will be

$$T_{\text{spec}} = 1 - R_1 - CR_1\{1 - \exp[-(4\pi\sigma/\lambda)^2]\}. \quad (17)$$

Very little of the diffusely transmitted light reaches the detector, because at short wavelengths it is strongly absorbed in the coating, and at long wavelengths it becomes small, roughly proportional to  $\lambda^{-2}$ , as indicated by an expansion of Eq. (13). The scattering parameter defined in Eq. (16) may be considered somewhat analogous to the anisotropy parameter<sup>24</sup> of Mie theory. By such analogy<sup>24,25</sup> one would expect that for  $\sigma \approx \lambda$ ,  $C > 1$ ; and for  $\sigma \ll \lambda$ ,  $C \approx 1$ . The value of  $C$  is constrained at short wavelength or large  $\sigma$  by the requirement that  $T_{\text{spec}}$  be positive, which leads to  $C < R_1^{-1} - 1$ .

Since this is a first-order analysis and since Eqs. (10) and (11) are scalar results, appropriate parts of those equations can be directly combined for the special case of normal incidence. The result in Eq. (11) can be applied directly to the first and third terms of Eq. (10) by

$$\begin{aligned} R_A = & R_1[\exp\{-(4\pi\sigma_1/\lambda)^2\} + (1 - \exp\{-(4\pi\sigma_1/\lambda)^2\})(1 - \exp\{-(\sqrt{2}\pi\alpha\sigma_1/m_1\lambda)^2\})] \\ & + 2 \cos(4\pi nd/\lambda) R_1^{1/2} T_{\text{spec}} \exp\{-(4\pi/\lambda)^2(\sigma_1^2 + \sigma_2^2)/2\} \exp\{-4\pi kd/\lambda\} \\ & + T_{\text{spec}}^2 \exp\{-8\pi kd/\lambda\} \exp\{-(4\pi\sigma_2/\lambda)^2\}. \end{aligned} \quad (19)$$

replacing  $R_1$  and  $R_2$  with appropriately notated forms of Eq. (11). The second term in Eq. (10) represents interference between the first and second surface reflections. Since only the specular reflectance from those surfaces has sufficient phase coherence to produce interference, the product  $(R_1 R_2)^{1/2}$  in Eq. (10) is replaced by the appropriately notated specular terms

$$\begin{aligned} R_B = & R_1 \exp\{-(4\pi\sigma_1/\lambda)^2\} \\ & + 2 \cos(4\pi nd/\lambda) R_1^{1/2} (1 - R_1) \exp\{-(4\pi/\lambda)^2(\sigma_1^2 + \sigma_2^2)/2\} \exp\{-4\pi kd/\lambda\} \\ & + (1 - R_1)^2 \exp\{-8\pi kd/\lambda\} [\exp\{-(4\pi\sigma_2/\lambda)^2\} + (1 - \exp\{-(4\pi\sigma_2/\lambda)^2\})(1 - \exp\{-(\sqrt{2}\pi\alpha\sigma_2/m_2\lambda)^2\})]. \end{aligned} \quad (20)$$

from Eq. (11). And, of course,  $T_{\text{spec}}$  is substituted for  $T_1$  in the second and third terms of Eq. (10). The final result is

$$\begin{aligned} R = & R_1[\exp\{-(4\pi\sigma_1/\lambda)^2\} + (1 - \exp\{-(4\pi\sigma_1/\lambda)^2\})(1 - \exp\{-(\sqrt{2}\pi\alpha\sigma_1/m_1\lambda)^2\})] \\ & + 2 \cos(4\pi nd/\lambda) (R_1 R_2)^{1/2} T_{\text{spec}} \exp\{-(4\pi/\lambda)^2(\sigma_1^2 + \sigma_2^2)/2\} \exp\{-4\pi kd/\lambda\} \\ & + R_2 T_{\text{spec}}^2 \exp\{-8\pi kd/\lambda\} [\exp\{-(4\pi\sigma_2/\lambda)^2\} + (1 - \exp\{-(4\pi\sigma_2/\lambda)^2\})(1 - \exp\{-(\sqrt{2}\pi\alpha\sigma_2/m_2\lambda)^2\})] \end{aligned} \quad (18)$$

with  $R_1$  and  $T_{\text{spec}}$  given by Eqs. (6) and (17), respectively. Recalling the several assumptions made above, it should be emphasized that this first-order result correctly pertains only to the normal incidence, specular reflectance for  $\lambda \geq \sigma$  of a thick uniform coating with normal Gaussian surfaces as measured by a detector subtending the half-angle  $\alpha$ .

The exponential absorption coefficient,  $4\pi k/\lambda$ , is written explicitly in Eq. (18). This simple functional form has been shown by Koike *et al.*<sup>15</sup> and Borghesi *et al.*<sup>26</sup> to be appropriate to the continuous absorption by carbon black, an ingredient present in many coatings as noted earlier. Hence this form is used throughout. A more complex form for  $k$  is necessary to describe an absorption-band structure.

Equation (18) is not only cumbersome, it has nine adjustable parameters relating to the coating. Fortunately, in most applications enough is known about one surface or the other to evaluate directly a few parameters and eliminate some terms. For coatings applied to metallic telescope baffles, one can immediately set  $N_0 = 1$  for air in Eq. (6) and  $R_2 = 1$  for metal.

#### A. Case A: Rough Top and Smooth Substrate

In this common case the metal substrate below the coating is sufficiently smooth that its diffuse reflectance can be neglected. Thus

If  $d$ ,  $\sigma_1$ , and  $\sigma_2$  are measured, an equation with only four adjustable parameters ( $n, k, m_1, C$ ) is left for case A.

#### B. Case B: Rough Substrate and Smooth Top

Because the upper surface is smooth its diffuse reflectance is neglected, which also eliminates  $C$  as an unknown parameter:

If  $d$ ,  $\sigma_1$ , and  $\sigma_2$  are measured, Eq. (20) contains only three adjustable parameters ( $n, k, m_2$ ).

#### C. Case C: Both Surfaces Rough

In this case the only simplification of Eq. (18) possible is to let  $R_2$  equal unity. This case implicitly assumes that the two roughness patterns are uncorrelated spatially.

#### D. Case D: Both Surfaces Relatively Smooth

Using the same arguments as above, Eq. (18) simplifies to

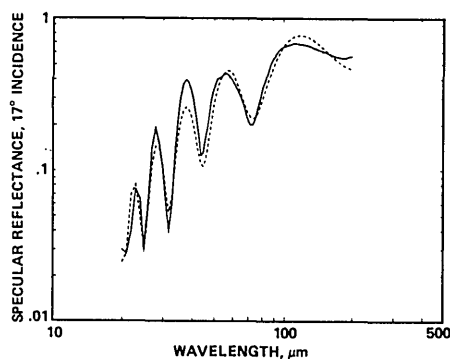


Fig. 6. Fit of the case A model (dashed) to the interferometric reflectance of Chemglaze Z-306.

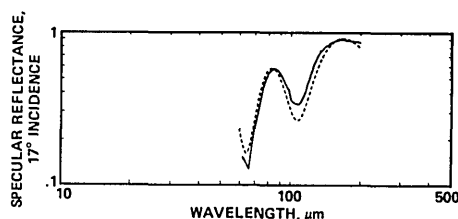


Fig. 7. Fit of the case A model (dashed) to the interferometric reflectance of ECP-2200.

$$R_D = R_1 \exp[-(4\pi\sigma_1/\lambda)^2] + 2 \cos(4\pi nd/\lambda) R_1^{1/2} (1 - R_1) \exp[-(4\pi/\lambda)^2(\sigma_1^2 + \sigma_2^2)/2] \exp[-4\pi kd/\lambda] + (1 - R_1)^2 \exp[-8\pi kd/\lambda] \exp[-(4\pi\sigma_2/\lambda)^2], \quad (21)$$

an equation with only two adjustable parameters ( $n, k$ ) when  $d$ ,  $\sigma_1$ , and  $\sigma_2$  are known. Of course, for very smooth surfaces this reduces to the thick film result given in Eq. (10).

## V. Comparison of Calculations with Measurements

In this section the model is fitted by a nonlinear least squares routine to the two sets of spectral data (interferometric and photometric) to determine the optical constants and surface parameters of six coatings. The uncertainty in the parametric values thus derived is estimated by a reduced chi-square technique, and the total error in the four most significant parameters is established for ambient and evacuated measurement conditions. Several different properties of the reflecting-layer model are demonstrated here by these diverse coatings.

The fitting routine (ZXSSQ of the International Mathematics and Science Library, Inc.) uses a finite difference Levenberg-Marquardt algorithm to determine the direction for parameter variation. Although this routine can handle many unknown parameters, we found it expedient to let the program adjust only two parameters at a time with best-estimate values used for the other parameters. The adjustable pair of parameters was then rotated among the unknowns until the sum of the squared residuals was minimized. Although nonunique solutions with grossly different parametric values were occasionally encountered, the independent

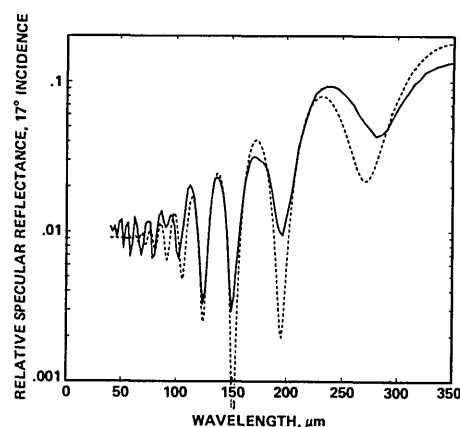


Fig. 8. Approximate fit of the single layer case D model (dashed) to the interferometric reflectance of the multilayer coating, LMSC.

measures of  $\sigma_1$  and  $d$  given in Table II always made clear which solution was physically reasonable. The value of  $\sigma_2$  used in most of these calculations,  $0.3 \mu\text{m}$ , was determined from profilometer measurements of representative substrates before coating.

### A. Interferometric Spectra

The case A model [Eq. (19)] was fitted by the above procedure to the interferometer spectra of Chemglaze and 3M ECP-2200. The model was not fitted to the ECP data at wavelengths below  $54 \mu\text{m}$  because there is no provision to describe the silicate absorption in that region. The calculated spectra, shown dashed in Figs. 6 and 7, show quite good agreement with the measurements indicating that the case A model is capable of at least a first-order representation of the reflectance from a single, approximately uniform, layer of rough thick coating material.

An attempt was also made to fit the case D model for smooth surfaces to the relative reflectance spectrum of the smooth multilayer coating LMSC (Fig. 8). At wavelengths about equal to the total thickness of the coating ( $200 \mu\text{m}$ ) the fit to the frequency of the data is fairly good. However, at shorter wavelengths—about the size of the individual layer thicknesses ( $\approx 50 \mu\text{m}$ )—the agreement between this model and the measurements is poor. This is not surprising since the single (thick) layer model does not account for (i.e., does



Table III. Optical Constants and Surface Parameters

Coating	Model	$n$	$k$	$\sigma_1$ ( $\mu\text{m}$ )	$m_1$ (deg)	$d$ ( $\mu\text{m}$ )	$C$	$\sigma_2$ ( $\mu\text{m}$ )	$m_2$ (deg)	rms residual (%)
Interferometer										
Chemglaze Z-306	A 106	1.37	0.066	2.3 (2)	1 <sup>a</sup>	41 (40)	0.4 <sup>a</sup>	0.3 <sup>a</sup>	—	17
3M ECP-2200	A 70	1.48	0.049	4.3 (4)	3 <sup>a</sup>	55 (55)	3 <sup>a</sup>	0.3 <sup>a</sup>	—	13
Photometer										
Chemglaze Z-306	A 8	1.38	0.117	1.6 (2)	0.6 <sup>b</sup>	30 (40)	0.4 <sup>a</sup>	0.3 <sup>a</sup>	—	20
IITRI D-111	A 8	1.62	0.32	3.0 (3)	3.3 <sup>b</sup>	61 (48)	0.9 <sup>a</sup>	0.3 <sup>a</sup>	—	30
3M ECP-2200	A 6	1.48	0.056	4.3 (4)	3 <sup>a</sup>	58 (55)	3 <sup>a</sup>	0.3 <sup>a</sup>	—	19
3M Black Velvet Nextel	A 5	1.37	0.34	10 (7)	8 <sup>a</sup>	70 (66)	6 <sup>a</sup>	0.3 <sup>a</sup>	—	20
Cornell	A 5	1.39	0.20	44 ( $\approx 30$ )	33 <sup>b</sup>	87 (96)	25	0.3 <sup>a</sup>	—	20
Martin	C 8	1.52	0.075	10 (8)	17 <sup>b</sup>	88 ( $>50$ )	4 <sup>a</sup>	10.9	1.2	18

Note: The same samples of Chemglaze and ECP-2200 were used in both kinds of spectral measurement.

<sup>a</sup> Parameter that has an insignificant effect on the fit of the model to these data.

<sup>b</sup> Parameter that affects the model fit at only the shortest waveband in the photometric data.

not resolve) the thinner individual layers of the multilayered coating. Undoubtedly a smooth multilayer model similar to that given by Heavens<sup>17</sup> or others could be fit to the measurements if the individual layer thicknesses were known.

The parametric values resulting from the minimization procedure are listed in Table III, where the values of  $\sigma_1$  and  $d$  measured by other means (Table II) are given in parentheses for comparison. The agreement found is generally encouraging, but some critical comments regarding the curve-fit to individual spectra will follow. The first column of Table III gives the case employed and number of data points fitted in each spectrum. As noted earlier,  $\sigma_2$  and  $m_2$  are adjustable parameters only in the case B and C models. The last column lists the rms residual (in percent) determined from the sum of the squared fractional residuals. The symbols *a* and *b* in the table indicate parameters which are only poorly determined because they were found to have an insignificant effect on the model fit. Four significant parameters,  $n$ ,  $k$ ,  $\sigma_1$ , and  $d$ , were found to strongly affect the fit of the case A model. In particular, when  $d$  is known, the frequency of fringes observed in these interferometric spectra unambiguously determines  $n$  through the frequency ( $4\pi n/\lambda$ ) of the cosine factor in the second term of Eq. (19).

## B. Photometric Spectra

Equation (18) is not our first model of the reflectance expected from a rough thick coating. An earlier version, which differed primarily by omitting the interference term, was fitted to three of the photometric data sets

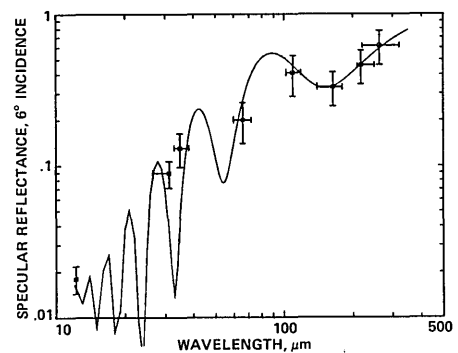


Fig. 9. Fit of the case A model to the photometric reflectance of Chemglaze Z-306.

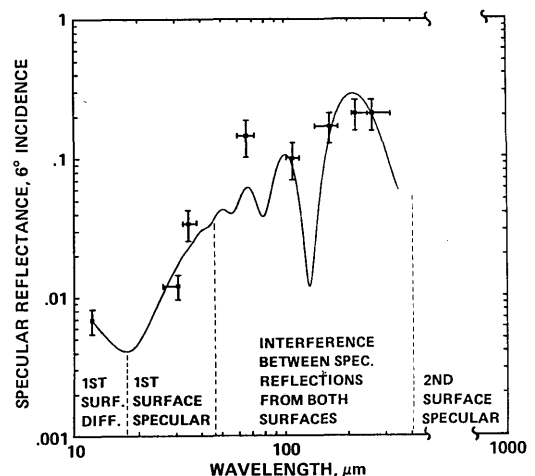


Fig. 10. Fit of the case A model to the photometric reflectance of IITRI D-111.

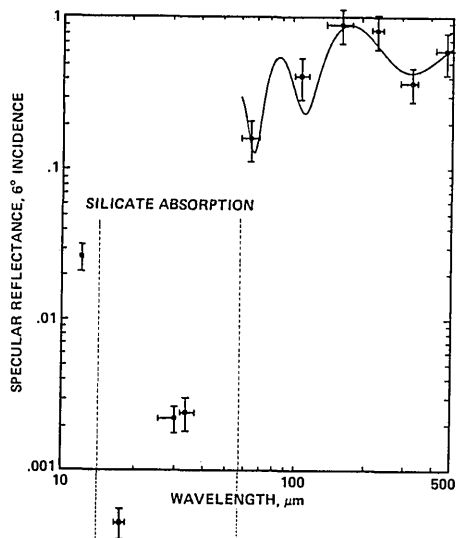


Fig. 11. Fit of the case A model to the photometric reflectance of 3M ECP-2200. The broad silicate absorption is indicated by dotted lines.

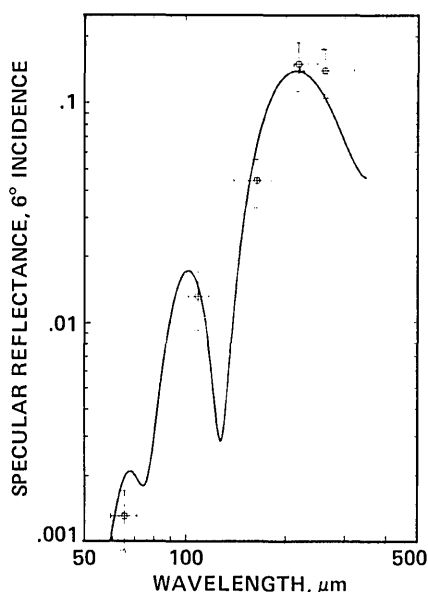


Fig. 12. Fit of the case A model to the photometric reflectance of 3M Black Velvet (Nextel 101-C10); note shift in ordinate scale.

with slightly smaller rms residuals than Eq. (18) produces. However, compared with the more detailed model described above, the early model produced significantly larger values of the optical constants. Similar values of  $\sigma_1$  are produced by the two models, however, which is consistent with  $\sigma_1$  being partly determined by the first term which was not changed. The most important difference between the two models is that the earlier one, which neglected interference effects, was totally incapable of fitting the photometric spectra of both Cornell Black and Martin Black.

It was shown in the previous section that the model can adequately represent the interference effects present in the interferometric spectra of three coatings; hence it seems permissible to let the least squares

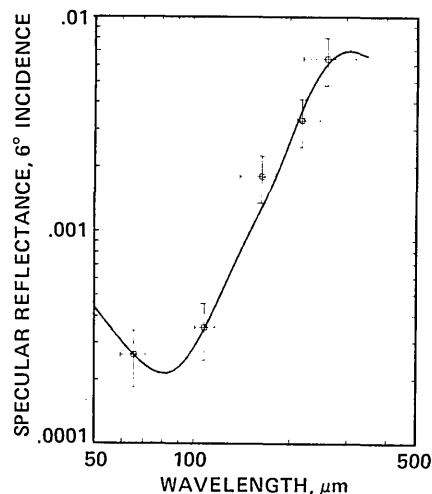


Fig. 13. Fit of the case A model to the photometric reflectance of Cornell Black; note shift in ordinate scale.

minimization routine utilize such fringes in fitting the model to the isolated data of photometric spectra. To do this, a 50-point average of the model is calculated across the effective passband of each filter, and the difference between these averages and the photometric data points  $M$  is minimized. The fractional residual,  $(\bar{R} - M)/M$ , was utilized to weight each data point equally. Because many of the fringes are relatively narrow, the effective passbands of each filter were re-evaluated on plots of  $\lambda^{-4}T$ . As a result, data from the lowest resolution filter ( $\Delta\lambda/\lambda = 83\%$  at the nominal peak wavelength of  $320 \mu\text{m}$ ) were found to produce too broad an average to be used in fitting the model. This reduced the number of photometric data points to a maximum of eight.

The fit of the case A model to the photometric measurements of two simple pigmented coatings is shown in Figs. 9 and 10, and the resulting parametric values are given in Table III. It was found during fitting that by adjusting the slope parameter  $m_1$  the model could nearly always be fitted to the data of the shortest-wavelength filter. Examination of Eq. (19) shows that  $m_1$  occurs only in the term describing the diffuse reflectance of the upper surface, so it can be deduced that the short-wavelength end of these spectra may contain a large diffuse contribution. Expanding the exponentials in the first term of Eq. (19) shows that the measured diffuse component has a  $\lambda^{-4}$  dependence; hence the slope on a log-log plot of the short-wavelength part of the spectrum will be the same whenever the diffuse component of the upper surface dominates the reflectance. The  $\lambda^{-4}$  decrease is so rapid, however, that the diffuse contribution seldom extends as far as  $30 \mu\text{m}$ . Quite often a minimum occurs in the calculated spectrum near  $20 \mu\text{m}$ , as in Fig. 10, where the specular reflectance from the upper surfaces rises above the diffuse contribution with increasing wavelength. In the absence of data at this minimum, the level of the short-wavelength reflectance calculation can be adjusted through  $m_1$  to fit almost any measured  $10\text{-}\mu\text{m}$  data

without affecting the longer-wavelength fit. This was used to reduce the number of adjustable parameters by one by not fitting the 10- $\mu\text{m}$  datum until after the longer-wavelength data had been fitted by adjustment of the other significant parameters. Then the 10- $\mu\text{m}$  datum was fitted by adjusting  $m_1$  alone.

The Chemglaze, IITRI, and Martin Black photometric data were treated in this manner. Applying this technique to the IITRI data may have been somewhat questionable since the sharp decrease of the IITRI spectrum below 60  $\mu\text{m}$  might be partly a result of absorption by the silicate material indicated in Table II. The different kinds of reflectance associated with the two surfaces of the model separate rather well in Fig. 10, and the approximate wavelength regimes that they dominate are indicated at the bottom of the figure. The ordering in wavelength is probably characteristic of many case A coatings.

A serious drawback of these photometric measurements is that there are not enough data to resolve a structure such as the diffuse-specular minimum described above. This criticism applies particularly to the interference fringes arising from the second term of Eq. (18). The strength of this term is largely determined by the parameters  $n$ ,  $k$ ,  $d$ , and  $\sigma_1$  in the case A model. Whereas  $n$  and  $d$  are primarily determined by the measured frequency of the fringes,  $k$  and  $\sigma_1$  are strongly affected by their depth. This is particularly true of  $\sigma_1$  at long wavelength since  $k$  appears at several places in Eq. (19). Hence  $\sigma_1$  is the significant parameter least well determined by the photometric study. Values found for it may be uncertain by as much as 45% (Chemglaze) when the peak-to-valley depth of the fringes is unknown. It is likely, therefore, that the apparent agreement in Table III between the calculated and profilometer-measured values of  $\sigma_1$  for IITRI D-111 is fortuitous.

The next three photometric spectra have one obvious feature in common: the very strong absorption between 18 and 38  $\mu\text{m}$ . This is shown for ECP-2200 in Fig. 11 and for 3M BV and Cornell Black in Fig. 3. The ECP data were not plotted in Fig. 3, because they were obtained at a different time with a gaseous  $\text{N}_2$  purge and with somewhat different filters. As noted earlier, all three of these coatings contain silicate material which has been shown to absorb strongly at these wavelengths. The data at wavelengths beyond the absorption feature are fitted by the case A model in Figs. 11–13. Since the model was not fitted to the 12- $\mu\text{m}$  data,  $m_1$  does not appear to be a significant parameter for either ECP-2200 or 3M BV.

The parametric values found by the minimization routine for these three coatings are consistent with the measurements and ingredients listed in Table II. Because 3M BV and Cornell Black have the same binder material, their optical constants ( $n, k$ ) should be quite similar. The somewhat different value of  $n$  found for ECP is consistent with a different binder, and the conspicuously small value of  $k$  compared with that of the other two coatings is what would be expected from the absence of carbon black in ECP.

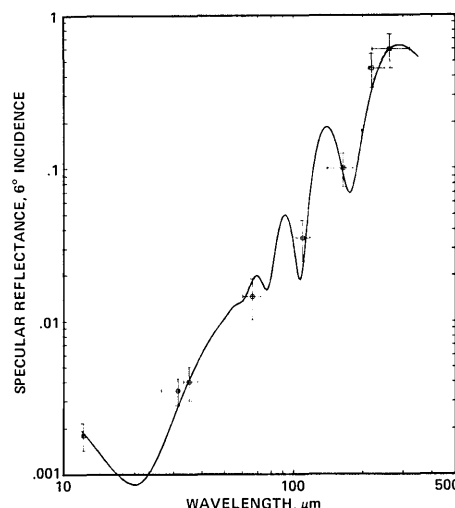


Fig. 14. Fit of the case C model to the photometric reflectance of Martin Black.

It is obvious from Table II that the important difference between 3M BV and Cornell Black is the inclusion of large particles of SiC grinding grit in Cornell Black. This has at least three important effects, two of which can be seen by comparing Figs. 12 and 13. First, the surface roughness  $\sigma_1$  of Cornell Black is increased by a factor of  $\sim 4$ , which damps out the longwave interference fringes from the model calculation and also creates a significant first surface diffuse contribution at 65  $\mu\text{m}$  (note the small minimum in the calculation near 85  $\mu\text{m}$ ). Second, the presence of the diffuse contribution makes  $m_1$  a significant parameter at 65  $\mu\text{m}$ . Third, the scattering parameter  $C$  becomes significant near 150  $\mu\text{m}$  because the long-wavelength side of the minimum is due to specular reflection from the lower surface. Cornell is the only coating measured to date for which  $C$  is important. From Eq. (17) one can see that at  $\lambda \gtrsim 100 \mu\text{m}$ ,  $\sigma_1$  must be  $> 15 \mu\text{m}$  for  $T_{\text{spec}}$  to be significantly reduced by diffuse transmission through the upper surface. The value of  $C$  that was found (25) falls just within the  $R_1^{-1} - 1$  range required to keep  $T_{\text{spec}}$  positive. Finally, the large difference in longwave reflectance between 3M BV and Cornell Black shown in Fig. 3 might suggest that there is a long-wavelength absorption in SiC. However, the literature<sup>16</sup> does not support such a speculation, and the case A model is apparently capable of explaining the very low specular reflectance on the basis of a large diffuse reflectance.

The only case C coating studied is Martin Black. According to Stephen Pompea (Martin-Marietta, Denver, Colo.) the aluminum substrate is roughened by a vapor-hone process with submillimeter size particles before being anodized. During anodization, material, which may be largely a form of aluminum oxide, builds up electrochemically on the roughened substrate. Characteristic thicknesses of the deposit range from 60 to 100  $\mu\text{m}$ . Scanning electron micrographs (Ref. 27 and our own) show that the upper surface of the deposit is composed of very steep-walled facets whose shape may best be described as elongated pyramids, tongues, or

Table IV. Chi-Square Uncertainty in Percent (Derived From Interferometer Spectra)

Coating	Model	$\delta n$	$\delta k$	$\delta \sigma_1$	$\delta d$
Chemglaze Z-306	A	1.8	9.2	36.0	2.0
3M ECP-2200	A	2.0	12.5	32.0	2.2

squat spires. These spires are packed together with a horizontal separation of the order of 15  $\mu\text{m}$  and a peak-to-valley depth of  $\sim 20 \mu\text{m}$ . Thus this description is that of a case C coating, and in Fig. 14 the best fit of the case C model to the photometric data is shown.

Because  $\sigma_1$  and  $\sigma_2$  are both so large, no specular reflection from either surface is apparent at wavelengths below 200  $\mu\text{m}$ . The minimum near 20  $\mu\text{m}$  in Fig. 14 is in this case due to the diffuse contributions from both surfaces, with the lower surface predominating on the long-wavelength side of the minimum, of course. At longer wavelengths (60–300  $\mu\text{m}$ ), the interference term dominates. It is reassuring that the fringes calculated in this region are quite similar to those measured by Pompea *et al.*<sup>28</sup> on a different sample, which they refer to as Martin Optical Black.

The rms residuals listed in Table III are less than the average photometric error bar (25%) in all but one case, implying that the model may be as good as the data. Although the photometric residuals do not indicate significance in a reduced chi-square test because of the small amount of data, an approximate reduced chi-square calculation using the interferometric residuals does indicate statistical significance when the expected value of the error distribution is  $\sim 15\%$ . Chi-square analysis shows theoretically that given the correct model, additional data reduce statistical uncertainty and result in a better fit. The better fit of the interferometric spectra is demonstrated in Table III by noticeably smaller residuals.

### C. Estimation of Error in Parametric Values

Experience fitting the reflecting-layer model to these spectra has already reduced the list of important parameters from the nine specified in Eq. (18) to the four without special notation in Table III. Equation (18) shows that the four significant parameters ( $n$ ,  $k$ ,  $\sigma_1$ , and  $d$ ) are not independently determined by the model. For example,  $\sigma_1^2$  and  $\sigma_2^2$  are weighted equally and are interchangeable within the interference term, while  $n$ ,  $k$ , and  $d$  are related through algebraic, trigonometric, and exponential factors.

A generally accepted technique for establishing the uncertainty in derived parametric values is to adjust one parameter by arbitrary amounts (and optimize the other parameters for a minimum chi-square) until the reduced chi-square has been increased by one from its minimum value. This corresponds to increasing the mean residual by  $\sim 1\sigma$  of a Poisson error distribution. Bevington<sup>29</sup> has shown that this produces a reasonable definition of the uncertainty for nonlinear as well as linear solutions. To reduce further the number of ad-

Table V. Total Estimated Error in Significant Parameters (Percent Error)

Condition	$\Delta n$	$\Delta k$	$\Delta \sigma_1$	$\Delta d$
Ambient	2	80	40	30
Purged or evacuated	2	15	35	2

justable parameters,  $\sigma_1$  and  $d$  were fixed at the measured values given in Table II, while the above technique was applied to the interferometric spectra of Chemglaze and ECP to find the uncertainties in  $n$  and  $k$ . To find the uncertainties in  $\sigma_1$  and  $d$ , the other parameters were fixed at their optimum values. The results in Table IV indicate that  $n$  and  $d$  are determined with considerable accuracy by the model fit, presumably because they determine the frequency of the interference fringes. As noted earlier,  $k$  and  $\sigma_1$  are closely associated with the peak-to-valley depth of the fringes. Figures 6 and 7 show that the peaks and valleys are not fitted by the model as well as the frequency, and this is reflected by the greater uncertainties found in  $k$  and  $\sigma_1$ .

When the uncertainties in Table IV are applied to the interferometer values listed in Table III good agreement is found with the values obtained by other means (Table II) and with the values found photometrically for ECP. However, for Chemglaze the photometrically determined values of  $k$  and  $d$  are far outside the chi-square uncertainties, and the value of  $\sigma_1$  differs from the interferometer value by nearly the full amount of the large uncertainty in that parameter. These differences contrast with the good agreement found between the interferometric and photometric values of  $n$  for Chemglaze; they are disturbing because they result from different kinds of measurement of the same sample.

Since the discrepancies just noted are associated only with the extinction parameters of the model, it is possible that they are due to different conditions at the upper surface of the Chemglaze sample during the photometer measurement. The photometry of Chemglaze was done with ambient laboratory conditions existing all along the optic path; the ECP photometry was obtained with a dry nitrogen gas purge, and the interferometry of both samples was done in an evacuated chamber. Thus, it is quite possible that more atmospheric water vapor remained adsorbed on the Chemglaze sample during its photometry than on the ECP sample, and certainly more than remained later on in the interferometer. This hypothesis is supported by the Chemglaze photometric reflectance data between 35 and 164  $\mu\text{m}$ , which run  $\sim 40\%$  below the interferometric spectrum (averaged over the filter passbands); on the other hand, the three ECP photometer data points in the same spectral region agree well with the interferometer spectrum. Calculations of the interference term of Eq. (19) (the dominant term near 100  $\mu\text{m}$ ) using the values of  $k$ ,  $d$ , and  $\sigma_1$  in Table III also confirm this observation, that is, the Chemglaze photometry is  $\sim 50\%$  low, but the purged ECP photometry is not. Because the absorption coefficient of water in the 100- $\mu\text{m}$  region<sup>30</sup> is so large, only minute amounts make a noticeable difference in transmission. This

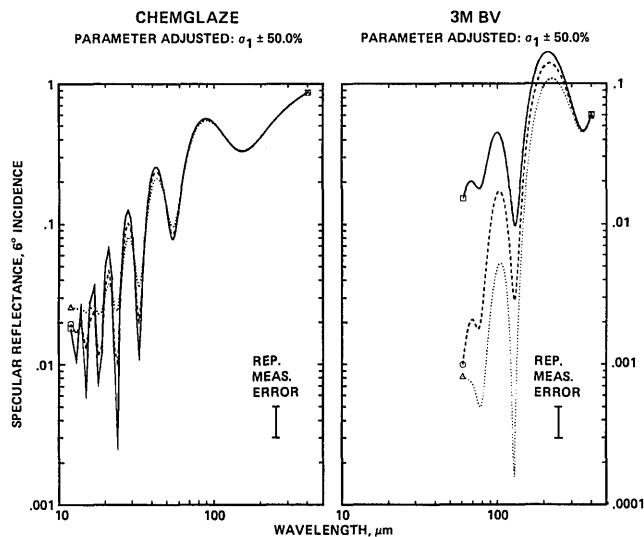


Fig. 15. Effect of varying parameter  $\sigma_1 \pm 50\%$  in the case A models of Chemglaze Z-306 and 3M Black Velvet; note different ordinate scales:  $\Delta = +50\%$ .

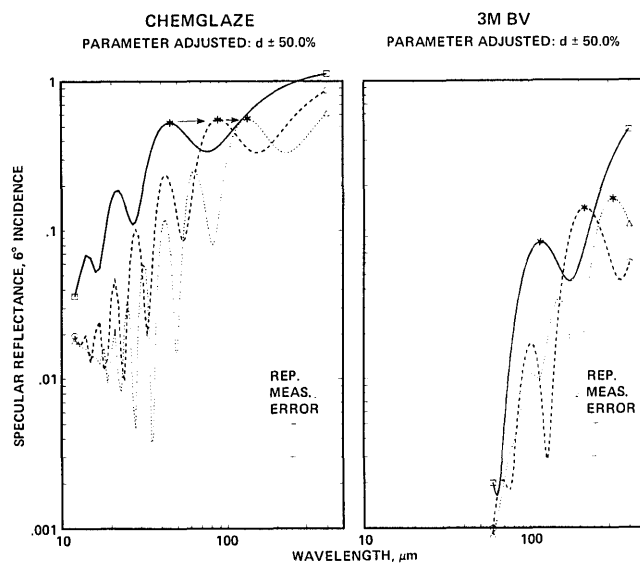


Fig. 17. Effect of varying parameter  $d \pm 50\%$  in the case A models of Chemglaze Z-306 and 3M Black Velvet; asterisks indicate a peak with constant phase:  $\Delta = +50\%$ .

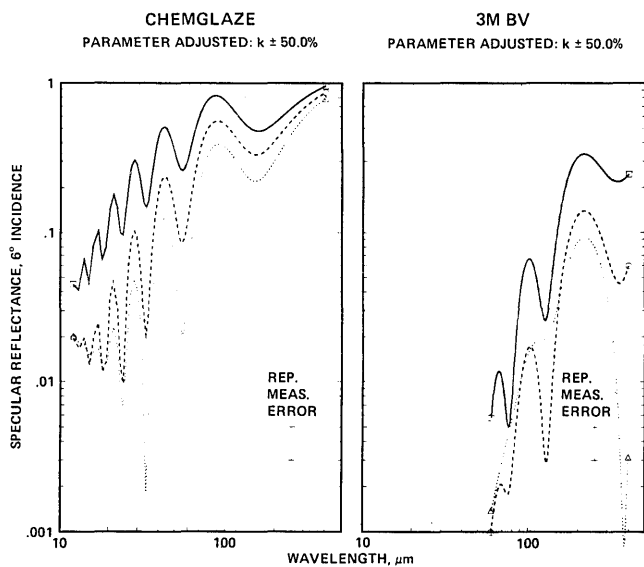


Fig. 16. Effect of varying parameter  $k \pm 50\%$  in the case A models of Chemglaze Z-306 and 3M Black Velvet:  $\Delta = +50\%$ .

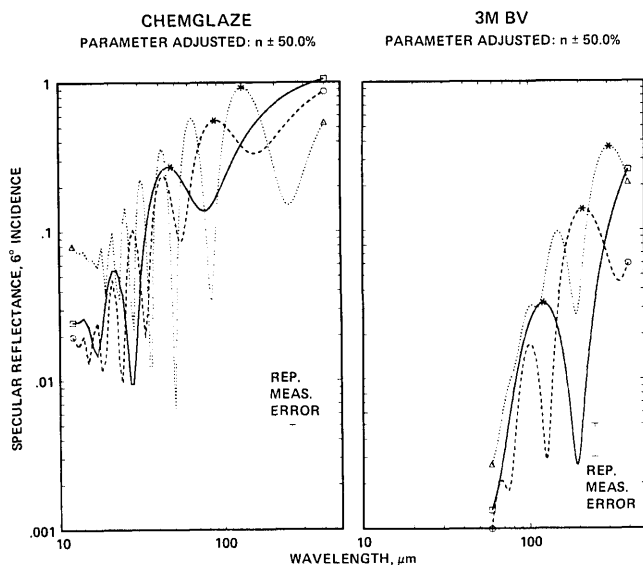


Fig. 18. Effect of varying parameter  $n \pm 50\%$  in the case A models of Chemglaze Z-306 and 3M Black Velvet; asterisks indicate constant phase:  $\Delta = +50\%$ .

residual water absorbed on the Chemglaze surface is a highly plausible explanation of the difference in the parametric values derived from fitting the model to the photometric and interferometer spectra of the Chemglaze sample. This hypothesis thus implies that the total error in  $k$  and  $d$  for measurements made under ambient conditions (all the photometry except ECP-2200) should be increased from the amounts indicated in Table IV to values closer to the differences found in the Chemglaze measurements (75% for  $k$  and 25% for  $d$ ). The total error in the significant parameters is estimated on this basis and listed in Table V. Future measurements should obviously be made under purged or evacuated conditions.

## VI. Sensitivity of the Model to Parameter Variation

Each parameter in the different models has been varied independently to determine its effect on the reflectance spectrum. The most general result is that the longest-wavelength spectrum is controlled by those parameters that lie the farthest below the upper surface and are contained in the third term of Eq. (18). The shortwave spectrum is controlled by parameters located at the upper surface and contained in the first term of Eq. (18), whereas most of the IR spectrum is dominated by interference fringes described in the second term of the equation and related to the significant parameters of both surfaces and the medium.

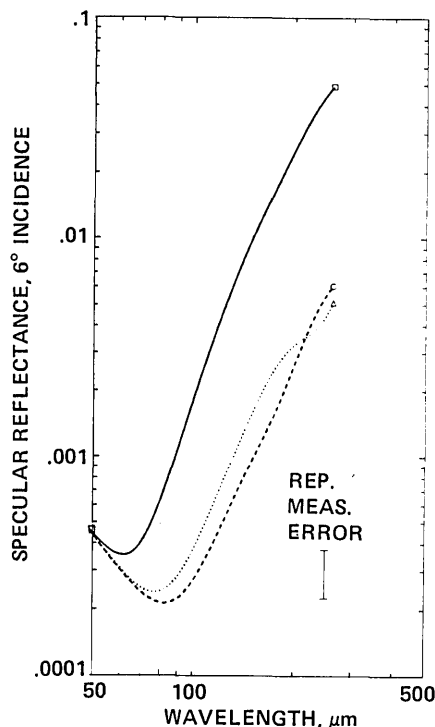


Fig. 19. Effect of varying parameter  $C \pm 50\%$  in the case A model of Cornell Black; note shift in ordinate scale:  $\Delta = +50\%$ .

Two examples, one thick and one thin, of the effect of independent variation of each of the four significant parameters of the case A model are examined in Figs. 15–18. In these figures, the best least squares fit to the photometry of the previous section is indicated by circles and dashed curves. The reflectance calculated with the specified parameter increased by 50% is marked by triangles and dotted curves, while that calculated with the parameter decreased 50% is marked by solid curves and squares. Unfortunately, Eq. (19) is so complex that even individual parameter variation often produces effects that result from various combinations of reflection at the upper surface, interference between the reflections from both surfaces, and absorption in the body of the coating. The more apparent case A effects will be decreased first, followed by comparisons with the case C model.

In Fig. 15, the effect of varying  $\sigma_1$  is pretty well isolated in the thick coating, 3M BV. Because the product  $kd$  is quite large, the third term (bottom surface) reflectance is negligible, and the second (interference) term is small. (Note that the total reflectance is also about one-tenth of that of the thin coating, Chemglaze.) Thus the first term (upper surface) dominates the reflectance through the exponential rise of its specular component as  $\lambda$  increases. The right-hand side of Fig. 15 clearly shows the inverse effect that  $\sigma_1$  has on the specular reflectance of 3M BV. This result can be contrasted with the oscillatory effect that variation of  $\sigma_1$  has on the thin coating, Chemglaze. In this thin-coating example  $kd$  is small enough that all terms contribute, and the second term is significant. This is

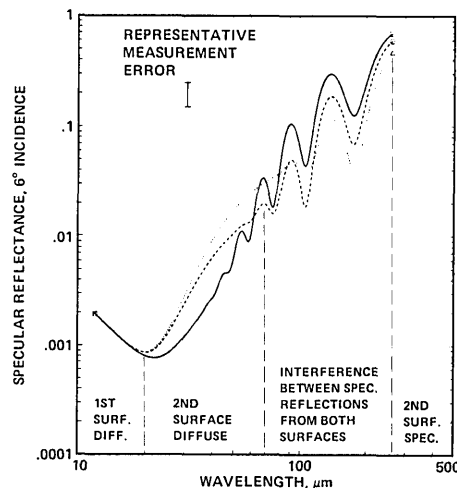


Fig. 20. Effect of varying parameter  $\sigma_2 \pm 50\%$  in the case C model of Martin Black:  $\Delta = +50\%$ .

demonstrated by the smaller amplitude of the interference fringes for larger values of  $\sigma_1$ , which causes the  $\pm 50\%$  curves to oscillate in relation to each other between the peaks and valleys. At the shortwave end of the Chemglaze spectrum note that (a) the interference fringes are nearly damped out for  $\sigma_1 + 50\%$ , and (b) the vertical order of the symbols that indicate parameter variation is opposite to that for 3M BV. This indicates that (a) the values of  $\sigma_1/\lambda$  and  $kd/\lambda$  are large enough to damp out the second term, and (b)  $\lambda$  is small enough for the diffuse component of the first term to dominate the reflectance of Chemglaze but not that of 3M BV.

In Fig. 16, the inverse dependence of total reflectance on  $k$  is clearly evident at mid- and long-IR wavelengths in the Chemglaze spectra where all terms contribute. In the 3M BV spectra, the effect is reversed for  $k + 50\%$  at the shorter wavelengths as the upper surface specular reflectance begins to dominate through an increase of  $R_1$ . This can occur for materials with optical constants where  $k \cong n - 1$ .

In Fig. 17, a decrease in total reflectance similar to that obtained by increasing  $k$  can be seen in the Chemglaze spectra with increasing  $d$ . However, this effect is partly masked by the concurrent increase in frequency of the interference fringes owing to the change in the cosine factor of the second term. To move with the interference peak as indicated by asterisks in Fig. 17, the change in  $\lambda$  must be the same as the change in  $d$ . Hence the attenuation due to  $kd/\lambda$  does not change. Thus in this coating, where  $\sigma_1$  is small and the interference term is important, the total reflectance at features of constant phase does not change significantly, with the result that an increase in  $d$  just shifts the fringe pattern to longer wavelengths. The shift is also apparent in the thicker coating but not at constant reflectance.

The effect of varying  $n$  is very complicated, as Fig. 18 shows. However, the frequency shift toward longer wavelengths is apparent. Staying at a feature of constant phase, such as the indicated peak, the total reflectance increases with  $n$  because both the wavelength

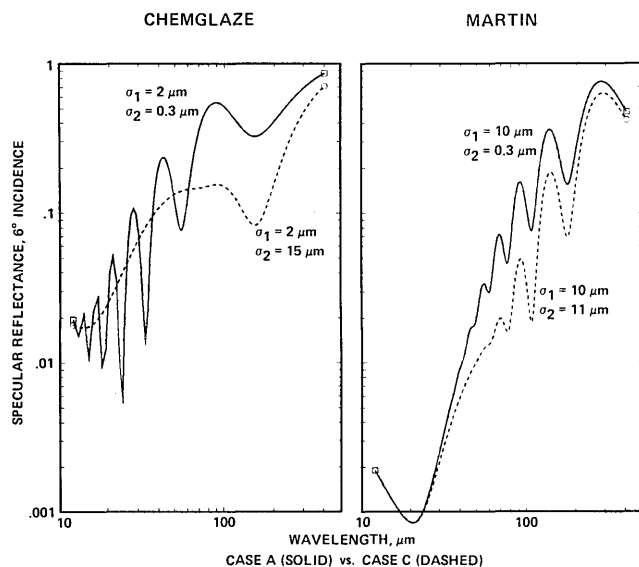


Fig. 21. Comparison of case A (solid) and case C (dashed) models in the coatings Chemglaze Z-306 and Martin Black.

and  $R_1$  increase. Although the general effect is complicated, the increased reflectance due to  $R_1$  is apparent at the shorter wavelengths through the diffuse component in Chemglaze and the specular component in 3M BV.

Cornell Black is the only coating studied in which the upper surface is rough enough that diffuse transmission through the upper surface detracts from the lower surface reflectance as indicated by Eqs. (17) and (19). Thus the case A model of Cornell Black has a strong inverse dependence on the scattering parameter, as shown by the curves for  $C$  and  $C - 50\%$  in Fig. 19. Considering the description (Table II) of this unusual coating, in which the major dimensions of the SiC particles are 2 or 3 $\times$  the average coating thickness, one may surmise that this inverse dependence on  $C$  must also be related to the large value of the slope  $m_1$  found for this coating. It was noted earlier that  $C$  is constrained to values  $< R_{11}^{-2} - 1$  by the physical requirement that  $T_{\text{spec}}$  be positive. With  $R_1 = 0.0334$ , as indicated by Table III and Eq. (6), this constraint is broken for  $C + 50\%$ . The anomalous result is then a direct dependence on  $C$ , which explains the crossover of spectra in Fig. 19.

In the case  $C$  model, the significant parameters are  $\sigma_2$ ,  $m_2$ , and the significant parameters of case A, variation of which produces effects in case  $C$  that are quite similar to those described above. The effects of varying  $\sigma_2$  in a thick case  $C$  coating, Martin Black, are shown in Fig. 20. Note that the reflectance between 20 and 70  $\mu\text{m}$  generally lacks interference fringes, has a positive slope, and has a direct dependence on the value of  $\sigma_2$ . These effects are due, respectively, to (a) the large values of  $d$ ,  $\sigma_1$ , and  $\sigma_2$ , which destroy the interference term at short wavelengths, (b) the diffuse reflectance of the lower surface which generally has a positive slope because of the absorption factor  $\exp(-8\pi kd/\lambda)$ , and (c) the second surface diffuse reflectance, which has a direct dependence on  $\sigma_2$ . This diffuse reflectance occurs at

these longer wavelengths because  $m_2 \ll m_1$ . The total reflectance in this region has a dependence on  $m_2$  opposite to that of  $\sigma_2$ , that is, inverse. In the region of interference fringes, variation of  $\sigma_2$  has effects similar to those shown in Fig. 15 for variation of  $\sigma_1$  in 3M BV as well as increasing the second surface diffuse reflectance at shorter  $\lambda$ . At the longest wavelengths, the inverse dependence on  $\sigma_2$  of the specular reflectance from the second surface begins to become apparent. In this case  $C$  example, the different kinds of reflectance associated with the two surfaces are separated rather well, and the regimes that they dominate are indicated at the bottom of Fig. 19, which can be compared with Fig. 10 for case A.

Finally, the gross variation of a model parameter can be used to examine the change in specular reflectance that would be expected from a change in coating design. For example, suppose the Chemglaze coating of Table III and Fig. 9 had been applied to a rough ( $\sigma_2 = 15\text{-}\mu\text{m}$ ) substrate instead of a smooth one. Assuming that all parameters remained the same except  $\sigma_2$ , the left side of Fig. 21 shows that the resultant case  $C$  reflectance (dashed) is not significantly different from the average case A reflectance at wavelengths below 60  $\mu\text{m}$ . This rather surprising result occurs because the gross increase in  $\sigma_2$  caused a similarly large increase in the diffuse reflectance from the second surface. From 70 to 250  $\mu\text{m}$ , there is a decrease in total reflectance, as expected, but beyond 300  $\mu\text{m}$  there is little difference since the reflectance (specular) comes from the second surface in both cases. The largest difference occurs at 150  $\mu\text{m}$  where an interference fringe happens to coincide with the diffuse-specular minimum in the second surface reflectance. The right-hand side of Fig. 21 provides a similar example in a coating where the first surface is rough enough that beyond 20  $\mu\text{m}$  most of the reflectance comes from the second surface. In this case, increasing the roughness of the second surface does noticeably reduce the total specular reflectance between 40 and 200  $\mu\text{m}$ .

## VII. Summary and Conclusions

A far-infrared filter photometer for measuring both specular and nonspecular reflectance has been described. Specular photometric spectra of seven optically black coatings measured near normal incidence on this instrument between 12 and 500  $\mu\text{m}$  have been presented as well as three corroborating spectra from a Fourier transform interferometer. Three of the photometric spectra appear to show the principal absorption bands of amorphous silicate material near 25  $\mu\text{m}$ . Near 100  $\mu\text{m}$ , there is almost a 3-order-of-magnitude difference between the specular reflectance of the most and the least reflective coatings. As suggested by preliminary theoretical considerations, the reflectance of all coatings measured increased with wavelength at a sufficiently long wavelength.

Inverse relationships observed between the measured reflectance and the coating roughness and thickness led to development of a reflecting-layer model. This model includes an interference term which allows it to fit the



so-called channel spectra produced by many coatings. The model was successfully fitted to the spectra of seven coatings, permitting the optical constants ( $n, k$ ) and surface parameters ( $\sigma_1, d$ ) to be derived. Parametric errors were estimated by a reduced chi-square analysis. It was found that an rms surface roughness  $\sigma_1$  of  $\sim 40 \mu\text{m}$  was necessary to suppress interference fringes at wavelengths below  $300 \mu\text{m}$ .

The parameters of the reflecting-layer model were varied individually to determine which of them control the reflectance in different spectral regions. In general the longest-wavelength spectrum is controlled by the roughness of the lower surface, and the shortwave spectrum is dominated by the roughness of the upper surface (in the absence of absorption bands). Most of the IR spectrum is controlled by interference fringes related to all the significant parameters ( $n, k, \sigma_1, d$ ) of the coating. Also the reflectance generally increases exponentially with wavelength as values of  $kd/\lambda$  and  $\sigma/\lambda$  become small. For many case A coatings (in which the diffuse reflectance of the lower surface is negligible), the dominant type of reflectance changes with increasing wavelength in the following characteristic order: first surface diffuse; first surface specular; interference between both surfaces; second surface specular.

Finally, it is hoped that this work will assist in development of a new IR opaque coating to replace 3MBV (Nextel), which is no longer produced.

The author is indebted to Stuart W. Bowen of Beam Engineering, Sunnyvale, Calif., for several helpful suggestions. He would also like to thank Michael W. Werner, Jeffrey N. Cuzzi, and Fred C. Witteborn of NASA Ames Research Center for their constructive criticism; Eric Pan, Peter Spencer, and Marion Legg for their considerable help with the computer graphics; and Richard V. Howitt of the Santa Barbara Research Center, Goleta, Calif., who patiently directed the interferometer group which produced the three corroborating spectra that had such an important effect on this work.

## References

1. M. Born and E. Wolf, *Principles of Optics* (Macmillan, New York, 1970), p. 630.
2. H. E. Bennett and J. O. Porteus, "Relation Between Surface Roughness and Specular Reflectance at Normal Incidence," *J. Opt. Soc. Am.* **51**, 1234 (1961).
3. S. M. Smith, "Far-IR Optical Black Bidirectional Reflectance Distribution Function (BRDF)," *Proc. Soc. Photo-Opt. Instrum. Eng.* **257**, 161 (1980).
4. Buckbee-Mears Co., St. Paul, Minn.
5. K. Sakai and T. Yoshida, "Single Mesh Narrow Bandpass Filters from the Infrared to the Submillimeter Region," *Infrared Phys.* **18**, 137 (1978).
6. S. E. Whitcomb and J. Keene, "Low-Pass Interference Filters for Submillimeter Astronomy," *Appl. Opt.* **19**, 197 (1980).
7. A. Mitsuishi, Y. Otsuka, S. Fujita, and H. Yoshinaga, "Metal Mesh Filters in the Far Infrared Region," *Jpn. J. Appl. Phys.* **2**, 575 (1963).
8. K. R. Armstrong and F. J. Low, "Far-Infrared Filters Utilizing Small Particle Scattering and Antireflection Coatings," *Appl. Opt.* **13**, 425 (1974).
9. J. R. Grammer, L. J. Bailin, M. D. Blue, and S. Perkowitz, "Absorbing Coatings for the Far Infrared," *Proc. Soc. Photo-Opt. Instrum. Eng.* **257**, 192 (1980).
10. J. L. Pipher and J. R. Houck, "Black Paints for Far-IR Cryogenic Use," *Appl. Opt.* **10**, 567 (1971).
11. D. L. Stierwalt, "Infrared Absorption of Optical Blacks," *Opt. Eng.* **18**, 147 (1979).
12. J. P. Compton, J. E. Martin, and T. J. Quinn, "Some Measurements of Outgassing Properties and Far-IR Reflectivities of Two Optical Blacks," *J. Phys. D.* **7**, 2501 (1974).
13. S. M. Smith, "Far-IR Reflectance of Optical Black Coatings," Sixth International Conference on IR and MM waves, 7-12, Dec. 1981, Miami Beach, Fla., IEEE Cat. 81CH1645-1 MTT (1981).
14. K. L. Day, "Further Measurements of Amorphous Silicates," *Astrophys. J.* **210**, 614 (1976).
15. C. Koike, H. Hasegawa, and A. Manabe, "Extinction Coefficients of Amorphous Carbon Grains from  $2100 \text{ \AA}$  to  $340 \mu\text{m}$ ," *Astrophys. Space Sci.* **67**, 495 (1980).
16. B. L. Lutz and J. A. Ryan, "Silicon Carbide: Its Ground State and Predicted Spectrum," *Astrophys. J.* **194**, 753 (1974).
17. O. S. Heavens, *Optical Properties of Thin Solid Films* (University Microfilms, Ann Arbor, Mich., 1964), p. 55.
18. J. O. Porteus, "Relation Between the Height Distribution of a Rough Surface and the Reflectance at Normal Incidence," *J. Opt. Soc. Am.* **53**, 1394 (1963).
19. W. W. Wendlandt and H. G. Hecht, *Reflectance Spectroscopy* (Wiley, New York, 1966), p. 298.
20. J. M. Elson and R. H. Ritchie, "Diffuse Scattering and Surface-plasmon Generation by Photons at a Rough Dielectric Surface," *Phys. Status Solidi (B)* **62**, 461 (1974).
21. J. M. Elson, "Infrared Light Scattering from Surfaces Covered with Multiple Dielectric Overlayers," *Appl. Opt.* **16**, 2872 (1977).
22. H. E. Bennett, "Scattering Characteristics of Optical Materials," *Opt. Eng.* **17**, 480 (1978).
23. F. E. Nicodemus, J. C. Richmond, J. J. Hsia, I. W. Ginsberg, and T. Limperis, "Geometrical Considerations and Nomenclature for Reflectance," *Natl. Bur. Stand. U.S. Monogr.* **160**, 11 (1977).
24. J. F. Hansen and L. D. Travis, "Light Scattering in Planetary Atmospheres," *Space Sci. Rev.* **16**, 527 (1974).
25. M. Podolak and R. E. Danielson, "Axel Dust on Saturn and Titan," *Icarus* **30**, 484 (1977).
26. A. Borghesi, E. Bussolletti, L. Colangeli, A. Minatra, and F. Rubini, "Absorption Efficiency of Submicron Amorphous Carbon Particles between  $2.5$  and  $40 \mu\text{m}$ ," *Infrared Phys.* **23**, 85 (1983).
27. J. F. Wade and W. R. Wilson, "Infrared Properties of a Highly Absorbing Surface," *Proc. Soc. Photo-Opt. Instrum. Eng.* **67**, 61 (1975).
28. S. M. Pompea, D. W. Bergener, D. F. Shepard, and S. Russak, "Preliminary Performance Data on an Improved Optical Black for Infrared Use," *Proc. Soc. Photo-Opt. Instrum. Eng.* **400**, (1983), Fig. 5.
29. P. R. Bevington, *Data Reduction and Error Analysis for the Physical Sciences* (McGraw-Hill, San Francisco, 1969), p. 243.
30. C. W. Allen, *Astrophysical Quantities* (Athlone, London, 1963), p. 126.